

# Kinetics, Mechanism, and Optimization Modeling of a Green LFP Delithiation Process Developed for Direct Recycling of Lithium-Ion Batteries

François Larouche,\* Frédéric Voisard, Kamyab Amouzegar, Georges Houlachi, Patrick Bouchard, Ashok Vlijh, and George P. Demopoulos\*



Cite This: *Ind. Eng. Chem. Res.* 2023, 62, 903–915



Read Online

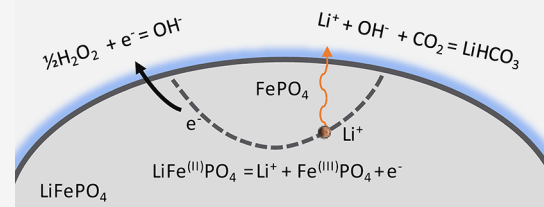
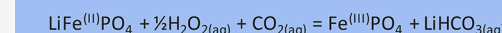
ACCESS |

Metrics & More

Article Recommendations

Supporting Information

**ABSTRACT:** Orthorhombic LiFePO<sub>4</sub> (LFP) offers highly reversible redox reactions, making it an attractive cathodic material for lithium-ion batteries. This electrochemical property was exploited to develop an environmentally benign selective lithium extraction process based on CO<sub>2</sub> and hydrogen peroxide that can be applied to direct LFP recycling. The proof of concept of this green delithiation process was demonstrated in a previously published paper, while the process optimization and the establishment of the reaction kinetic mechanism are addressed in the current paper. First, the effects of solid to liquid ratio (S/L), temperature, CO<sub>2</sub> pressure, and initial H<sub>2</sub>O<sub>2</sub> to LFP molar ratio were studied through an orthogonal design of experiments. In the range of conditions studied and considering the objective of maximizing the S/L ratio, the optimal conditions are a temperature of 20 °C, a CO<sub>2</sub> pressure of 2 atm, and a H<sub>2</sub>O<sub>2</sub> to LFP molar ratio of 1.25. In addition, reaction kinetic models were used to determine the reaction mechanism. The activation energies obtained based on rate constants from shrinking core and Avrami models are 15.7 and 13.9 kJ mol<sup>-1</sup>, respectively. While these values reveal a mixed or diffusion-controlled heterogeneous reaction, the analysis of half-delithiated LFP particles under scanning-transmission electron microscopy revealed the reaction being controlled by nucleation rather than diffusion. In this context, the Avrami model that accounts for nucleation and growth in solid-state reactions proved the most appropriate. Further, the reaction mechanism is concluded to be limited by nucleation of FP phase within the body of LFP during the early reaction stage and to sequentially shift to the one-dimensional diffusion-limited crystallite growth regime. Finally, it is shown that CO<sub>2</sub> acts as a buffering agent by neutralizing the LiOH formed by Fenton-like reactions between H<sub>2</sub>O<sub>2</sub> and ferric iron in LFP.



## 1. INTRODUCTION

Since its development and commercialization about 20 years ago, LiFePO<sub>4</sub> (LFP) has been extensively studied to improve its electrochemical performance. In particular, many mechanistic studies and modeling works have been performed to elucidate the charge transfer, diffusion, and phase transformation phenomena governing the LFP redox system. In this respect, many research groups proposed mechanisms based on a core–shell model as initially postulated by Goodenough,<sup>1</sup> followed by Laffont's expanding core model<sup>2</sup> and Srinivasan's shrinking core model.<sup>3</sup> Inversely, Delmas's group suggested a Domino-Cascade single-particle model based on lithium diffusion parallel to the interface between single phase LFP and FP domains. In nanosized particles, this leads to a fast propagation of a reaction front making crystallites grow much faster than the phase nucleation.<sup>4</sup> A hybrid model delithiation kinetics was proposed by Zhou's group featuring at the start of the process the domino cascade behavior subsequently changing to core–shell behavior.<sup>5</sup> Other groups embrace a broader multiparticle vision to explain the delithiation and lithiation mechanisms. Specifically, Zaghib proposed a mosaic

mechanism where each particle is a single domain,<sup>6</sup> while Bai and Tian integrated a statistical kinetics parameter to a model inspired from Avrami equation that considers an asynchronous transformation of all LFP particles.<sup>7</sup> Whichever the kinetic model selected, the lithium internal diffusion is always an important step of the mechanisms proposed, although nucleation has also been considered by some authors as the limiting mechanism. In this respect, Sumanov proposed a hybrid model based on potentiostatic measurements taking into account the chemical reaction limitations from both nucleation and diffusion.<sup>8</sup> These findings highlight the ambivalent mechanistic complexity of LFP, which would be limited by nucleation at a low current density but would

Received: October 1, 2022

Revised: November 10, 2022

Accepted: November 21, 2022

Published: January 4, 2023



become limited by diffusion at high charge/discharge rates. For an LFP sample having a similar morphology and particle size as the one used in the current study, Sumanov derived a diffusion coefficient of about  $2 \cdot 10^{-12} \text{ cm}^2 \cdot \text{s}^{-1}$ .<sup>8</sup>

Compared to complete dissolution method, selective lithium extraction is a highly attractive process to recycle LFP batteries due to its low cost, its reduced waste generation, its lower consumption of reagents, and the possibility of refunctionalizing the recovered  $\text{FePO}_4$ .<sup>9</sup> This green extraction approach has been studied in recent publications in which a selective leaching agent composed of organic acids<sup>10–13</sup> or inorganic acids<sup>14–16</sup> combined with an oxidant (usually  $\text{H}_2\text{O}_2$  or  $\text{Na}_2\text{S}_2\text{O}_8$ ) is employed to extract the lithium from LFP. In a previous paper,<sup>17</sup> we demonstrated the effectiveness of a novel chemical delithiation process for LFP that has the potential to be applied as an economical solution for LFP battery refunctionalization and recycling. This new process uses  $\text{CO}_2$  and  $\text{H}_2\text{O}_2$  as complexing and oxidizing green aqueous reagents to selectively extract the lithium from the carbon-coated LFP at circumneutral pH while keeping intact the orthorhombic structure of iron phosphate.<sup>17</sup> In this green process, the final products obtained are a  $\text{LiHCO}_3$ -rich aqueous solution that can be ultimately used to precipitate  $\text{Li}_2\text{CO}_3$  and a clean carbon-coated  $\text{FePO}_4$  (FP) suitable for reuse in Li-ion batteries.<sup>17</sup> The process still requires elucidation of the underlying kinetic mechanism and optimization to improve the Li extraction efficiency while maximizing the solid-to-liquid ratio, which is the subject matter of the present paper.

More specifically, in this paper, a multi-pronged in-depth analysis is undertaken aiming at reaction mechanism elucidation and process optimization. At first, a fractional factorial design of experiments (DOE) is applied to determine the effects of solid-to-liquid ratio, temperature, initial  $\text{H}_2\text{O}_2$  to LFP molar ratio, and  $\text{CO}_2$  partial pressure on four responses. In this respect, the DOE allows to significantly improve the lithium recovery compared to the results from the previous study.<sup>17</sup> Second, reaction kinetics are investigated by comparing different kinetic models to understand the mechanisms and the limiting reaction steps. The kinetic modeling results are substantiated via ex situ characterization by X-ray diffraction spectrometry (XRD) and scanning-transmission electron microscopy (STEM) of pristine and partially reacted samples.

## 2. EXPERIMENTAL SECTION

**2.1. Materials.** The experiments were conducted using a commercial carbon-coated LFP material produced by Phostech plant in Quebec formerly owned by Süd-Chemie and now Johnson Matthey. The composition of the initial sample, shown in the Supporting Information (Tables S1 and S2), was determined in a previous publication by reconciliating data from chemical assays, carbon analysis, loss on ignition, and XRD. The carbon-coated LFP adopts an elongated potato shape with a median particle size of 449 nm<sup>17</sup> and a length-to-diameter ratio of about 2.5.

**2.2. Design of Experiments.** To determine the most important factors influencing the delithiation of LFP, a fractional factorial DOE was realized. A series of responses including the extraction of Li, the Li concentration in the final solution, the residual Li concentration in the final solid, and the molar rate of  $\text{H}_2\text{O}_2$  consumption per mol of LFP were correlated to the solid-to-liquid ratio (S/L), the  $\text{CO}_2$  pressure, the temperature, and the molar ratio of  $\text{H}_2\text{O}_2$  to LFP in the

initial sample. The fractional design was composed of four factors evaluated at two levels with three center points. The total number of experiments ( $I$ ) is  $I = 2^{4-1} + 3 = 11$ . The order of experimentations was randomized.

The experimental procedure was very similar to exploratory tests described in a previously published paper,<sup>17</sup> except that the temperature was maintained by circulating a cooling 50% water glycol mixture in a coil immersed in the suspension. The pH of the slurry was initially adjusted to 6 with diluted sulfuric acid and left uncontrolled during experiments, stabilizing between 6.4 and 7.5. After filtration, samples were tested for pH and oxidation-reduction potential (ORP) and then sent for  $\text{H}_2\text{O}_2$  titration with  $\text{KMnO}_4$  and chemical assays (ICP-OES Agilent). At the end of the test, the solid product was subjected to XRD and fire assay. The list of tests with their factors is presented in Table S3 in the Supporting Information. To observe the phase changes during the delithiation test, samples from Test S-05 were subjected to XRD after filtration, washing, and drying.

### 2.3. Kinetic Experimentation Setup and Procedure.

The kinetic behavior was established through a series of tests at five different temperatures (10, 17.5, 25, 32.5, and 40 °C), five different initial molar ratios of  $\text{H}_2\text{O}_2$  to LFP (0.56, 0.8, 1, 1.2, and 1.4), two agitation speeds (600 and 1200 rpm), and two pressures of  $\text{CO}_2$  (2 and 0.66 atm). All experimental conditions are summarized in Table S4 in the Supporting Information. The experimental protocol was similar to the DOE protocol described earlier, except that  $\text{H}_2\text{O}_2$  was added in several times during the experiment in order to maintain as much as possible a constant concentration of peroxide in the reactor. In this respect, the initial  $\text{H}_2\text{O}_2$ /LFP molar ratio was set to 0.56, slightly above the stoichiometry. The sampling interval was shortened to provide enough data for kinetics analysis. A constant flow of  $\text{CO}_2$  was sparged in the slurry, and the temperature and  $\text{CO}_2$  pressure were carefully maintained constant. The S/L ratio was set at 0.5:100 w/w.

For each test, demineralized water was needed and was first deoxygenated by sparging nitrogen for 20 min. The LFP sample was wetted with the deoxygenated water in a nitrogen-filled glovebox prior to be dispersed with an ultrasonic probe for 3 min. A 2 mol  $\text{L}^{-1}$  phosphoric acid solution was used to adjust the pH.

**2.4. Calculation of Recovery and Selectivity.** The extraction percentage “ $x$ ” of element “ $i$ ” at time “ $t$ ” (min) is calculated for each individual time unit element “ $n$ ” from the incremental concentration in solution over the Li in solid fed this time unit element

$$x_i^n = \left\{ \left[ C_{i \text{ out}}^n \left( V^0 + \sum_{j=0}^n V_r^j - \sum_{j=0}^{n-1} V_s^j \right) - C_{i \text{ in}}^n \times \left( V^0 + \sum_{j=0}^{n-1} V_r^j - \sum_{j=0}^{n-1} V_s^j \right) \right] / [c_i^n w^n] \right\} \quad (1)$$

with  $C_{i \text{ out}}^n$  and  $C_{i \text{ in}}^n$  being the elemental aqueous concentration at time element “ $n$ ” in  $\text{g L}^{-1}$ ,  $V^0$  the initial volume of solution in L,  $c_i^n$  the elemental assay of the solid in %, and  $w^n$  the mass of the solid sample in gram entering the time element “ $n$ ”.  $V_r$  and  $V_s$  are respectively the volume of reagent added and sample retrieved. The suspension is considered homogeneous. The denominator term was estimated from the initial composition

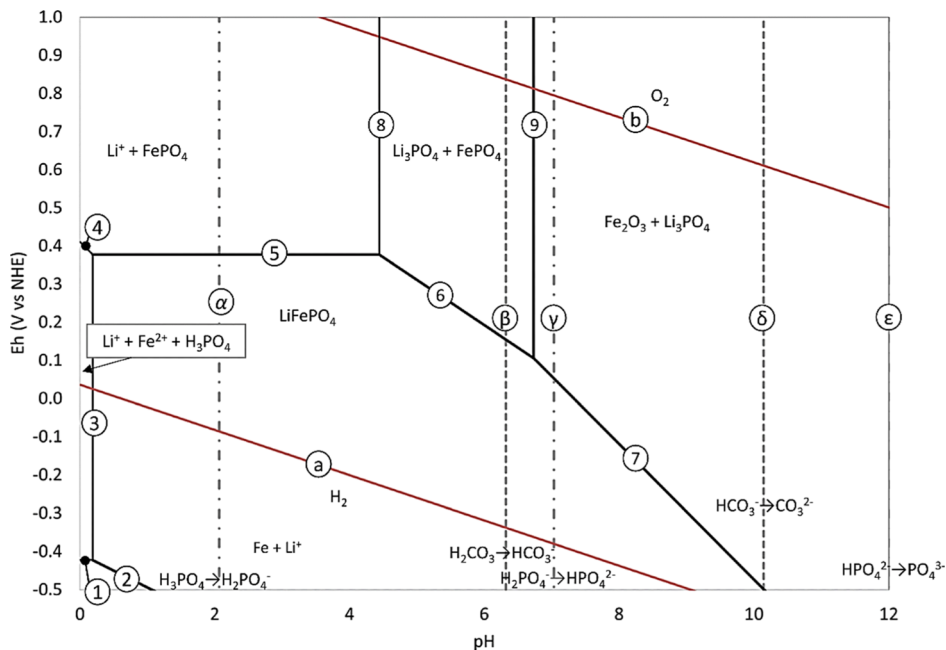


**Figure 1.** Predominant diagram of Fe in Li–Fe–P–CO<sub>2</sub> system at 298 K. The CO<sub>2</sub> pressure has been set to 2 atm; the molar activity of Li–Fe–P was set to 0.6 M each. The activity coefficient has been estimated with Davies's equation for ionic species.

and weight of sample times one minus the cumulative recovery of element “*i*” ( $X_i$ ) to the solution

$$c_i^n w_i^n = c_i^0 w_i^0 (1 - x_i^{n-1}) \quad (2)$$

The cumulative elemental recovery is calculated by multiplying the elemental recovery at time unit “*n*”

$$X_i^n = 1 - \prod_{j=0}^n (1 - x_i^j) \quad (3)$$

The relative error values on the recovery were estimated with the geometrical average of the standard deviation on chemical assays and the relative analytical and measurement error.

The model fitting for the DOE was done using a home-made MATLAB (2018a) program based on the Regress function. A sample of the program is available in the [Supporting Information](#). The statistical analysis of model parameters was based on ANOVA at 95% confidence level, regression coefficient of determination ( $R^2$ ), and the residual analysis.

**2.5. Characterization Methods.** **2.5.1. Chemical Analysis of Solutions.** Concentrations of Li, Fe, and P from solutions were determined with an inductively coupled plasma spectrometer (ICP-OES Perkin Elmer Optima 8300) in a 5% v/v HCl and 5% v/v HNO<sub>3</sub> solution matrix.

**2.5.2. Chemical Assays of Solids.** The determination of solid sample chemical composition was performed by first calcining the samples in air in an alumina crucible at 600 °C for 1 h and then at 850 °C for 4 h in a muffle furnace. Obtained calcined samples were first leached in concentrated HCl (acid to sample v/w ratio 30:1) at 80 °C for 1.5 h, followed by a second 4 h leaching at 90 °C after addition of concentrated HNO<sub>3</sub> (acid to sample v/w ratio 10:1). The final solution was diluted to obtain a 5% v/v HCl and 5% v/v HNO<sub>3</sub> solution matrix.

**2.5.3. X-ray diffraction spectrometry.** All XRD analyses had been performed on a MiniFlex 300 (Rigaku) diffractometer

equipped with a Co-K $\alpha$  source ( $\lambda = 1.79$  Å; 40 kV; 15 mA; scintillation counter SC-70 detector) from  $2\theta = 10$  to 120° in a step of 0.02°. Data were collected with Smartlab Studio (Rigaku) and analyzed with PDXL2 with ICDD PDF-4+ database. Phase quantification was done through Rietveld quantification.

**2.5.4. Brunauer–Emmett–Teller Measurement.** Brunauer–Emmett–Teller (BET) specific surface area measurements were performed using a QuadraSorb Quantachrome Instrument in N<sub>2</sub> (77.3 K). Each analysis was done in triplicate.

**2.5.5. Scanning–Transmission Electron Microscopy and EELS.** Observation of the samples by transmission electron microscopy (TEM) was done on a Hitachi HF 3300 S-TEM, equipped with a Gatan GIF Quantum ER energy filter and spectrometer. Several particles were deposited on a copper grid with a lacey carbon support film. The microscope can operate at beam energies of 60, 100, 200, and 300 keV. In this experiment, the microscope is operated at 300 keV, which is the optimal operation energy of this instrument. The microscope was operated in the scanning mode so that a spectral image can be recorded. The feature of interest for this study is the lithium-K and iron-M ionization edges. Although these ionization edges overlap each other, they show very different fine structures. The fine structure of the lithium-K edge is highly dependent on the chemical bonding of the lithium atom. The Li-K edge onset in LFP is located at 55 eV and consists of several small peaks over 5 eV s. The Fe-M edge onset is located at 57 eV and consists of a simple peak.

### 3. RESULTS AND DISCUSSION

**3.1. Pourbaix Diagram.** To verify the chemical reaction from a thermodynamic perspective, an  $E_h$ -pH diagram (Pourbaix diagram) of iron species for the system Li–Fe–P–H<sub>2</sub>O–CO<sub>2</sub> was plotted (Figure 1). The concentration of Li, Fe, and P was fixed at 0.6 M each, which corresponds to an LFP to water weight ratio of 1:10. Calculations were based on a pressure of CO<sub>2</sub> of 2 atm and a temperature of 298 K. In

**Table 1.** Experimental Results from the Orthogonal Experimental Design Including the Variable Conditions

test no	variables				responses <sup>a</sup>				normalized rate of H <sub>2</sub> O <sub>2</sub> consumption [mol H <sub>2</sub> O <sub>2</sub> min <sup>-1</sup> (mol LFP) <sup>-1</sup> ] ±9%
	S/L weight ratio X <sub>1</sub>	CO <sub>2</sub> pressure (atm) X <sub>2</sub>	temperature (°C) X <sub>3</sub>	H <sub>2</sub> O <sub>2</sub> /LFP molar ratio X <sub>4</sub>	final Li <sup>+</sup> concentration in solution (mg L <sup>-1</sup> ) ±3%	Li extraction (%) ±6%	Li grade in FP product (w/w %) ±7%		
S-1	1/100	4	40	0.75	445	100	0.22	0.055	
S-2	10/100	2	40	0.75	3655	83	1.02	0.093	
S-3	1/100	4	20	1.25	460	≈100 (103)	0.17	0.051	
S-4	5.5/100	3	30	1	2356	97	0.24	0.079	
S-5	5.5/100	3	30	1	2378	97	0.25	0.124	
S-6	10/100	2	20	1.25	4625	≈100 (104)	0.29	0.165	
S-7	1/100	2	40	1.25	437	98	0.17	0.061	
S-8	10/100	4	40	1.25	3525	79	1.19	0.233	
S-9	1/100	2	20	0.75	417	93	0.19	0.053	
S-10	10/100	4	20	0.75	4288	96	0.33	0.002	
S-11	5.5/100	3	30	1	2284	93	0.28	0.088	

<sup>a</sup>The relative uncertainty corresponds to the analytical variability.

**Table 2.** Main Statistical Effect for Selective Leaching of LFP as a Function of Variables and Their Model Equation<sup>a</sup>

response	significant factors		equation and coefficient of determination
	variables	2nd-order interaction	
Li <sup>+</sup> concentration in solution (mg/L)	X <sub>1</sub>		$Y_1 = \beta_0 + \beta_1 X_1 + \beta_2 X_3^2$ $R^2 = 99.5$
Lithium extraction (%)	X <sub>1</sub>	X <sub>1</sub> X <sub>3</sub>	$Y_2 = \beta_0 + \beta_1 X_1 + \beta_2 X_3 + \beta_3 X_1 X_3$ $R^2 = 88.3$
Li grade in FP product (w/w %)	X <sub>1</sub>	(X <sub>1</sub> X <sub>3</sub> ) <sup>2</sup>	$Y_3 = \beta_0 + \beta_1 X_1 + \beta_2 X_3 + \beta_3 X_1 X_3^2$ $R^2 = 99.1$
Normalized rate of H <sub>2</sub> O <sub>2</sub> consumption (mol H <sub>2</sub> O <sub>2</sub> min <sup>-1</sup> (mol LFP) <sup>-1</sup> )	X <sub>1</sub>	X <sub>1</sub> X <sub>3</sub>	$Y_4 = \beta_0 + \beta_1 X_1 + \beta_2 X_3 + \beta_3 X_4 + \beta_4 X_1 X_3 + \beta_5 X_1 X_4$ $R^2 = 96.4$
	X <sub>3</sub>	X <sub>1</sub> X <sub>4</sub>	
	X <sub>4</sub>		

<sup>a</sup>X<sub>1</sub> = S/L ratio, X<sub>3</sub> = temperature, X<sub>4</sub> = H<sub>2</sub>O<sub>2</sub>/LFP molar ratio.

such conditions, the solubility of CO<sub>2(aq)</sub> was estimated to 0.067 M based on tabulated data from Perry's Handbook of Chemical Engineering.<sup>18</sup> The Pourbaix diagram shows the predominant iron species found in the system at various conditions of pH and potential. The stability limits of water are indicated with red lines (lines "a" and "b"). For reference purposes, dashed lines indicating the speciation of soluble phosphates and soluble carbonates were added. Each line is identified with a number or a letter, which is associated to a chemical reaction. Details of the procedure, equations, and thermodynamic data used to build the diagram are provided in the Supporting Information. Thermodynamic data for bicarbonate salts (Fe and Li) were not available in the literature, and therefore, they have not been considered in the calculation. All calculations were done on Excel.

The obtained diagram shows similarities with the one developed by Jing et al.<sup>19</sup> with a large stability window for LiFePO<sub>4</sub> in the low acidic region, the predominance of ferric phosphate phase in upper left corner, the occurrence of a ferric oxide/hydroxide and Li<sub>3</sub>PO<sub>4</sub> in the right upper region, and the predominance of Fe(OH)<sub>2</sub> with Li<sub>3</sub>PO<sub>4</sub> in alkaline and reducing conditions. However, some notable differences can be observed. First, the stability region for LiFePO<sub>4</sub> is much smaller in Qiankun study because of a lower value for Gibbs energy of formation for this compound. They considered strengite as ferric phosphate compound, while we determined heterosite to be thermodynamically favored. Similarly, they considered Fe(OH)<sub>3</sub> instead of Fe<sub>2</sub>O<sub>3</sub> as ferric oxide

compound, which can be justified in terms of kinetics. He et al. proposed the thermodynamic stability window of LFP to be between pH 0 and 11.3,<sup>20</sup> in agreement with what we suggest (pH = 0.3 to 10.9) in similar conditions.

The diagram shows that LFP can be directly oxidized to FP between pH 0.5 and 6.7 at a potential above 369 mV vs SHE. When the pH is too basic, the LFP gets oxidized to Fe<sub>2</sub>O<sub>3</sub>, while lithium tends to precipitate as Li<sub>3</sub>PO<sub>4</sub>. However, considering the kinetic aspects of the reaction, it is more probable to find ferric oxyhydroxide (FeOOH) instead of Fe<sub>2</sub>O<sub>3</sub>. This can influence the diagram and expand the stability of LFP. On the other hand, when exposed to water, the LFP tends to form a protective hydrophobic layer of FP, as suggested by Zaghib et al.,<sup>21</sup> which will limit the phase transformation.

**3.2. Optimization of Process Parameters.** In a previous publication, the chemical delithiation in CO<sub>2</sub> and H<sub>2</sub>O<sub>2</sub> aqueous system was demonstrated, reaching up to 95% Li extraction at an S/L ratio of 1:100. However, increasing the solids loading in suspension caused the extraction to drop down to 85%.<sup>17</sup> The effect of various parameters is studied here through a fractional DOE with the objective to maximize the concentration of Li in solution and the lithium recovery and to minimize the residual Li concentration in the FP product as well as the consumption rate of H<sub>2</sub>O<sub>2</sub> normalized to the S/L ratio. The parameters studied and their range of values explored are the temperature from 20 to 40 °C, the S/L ratio from 1:100 to 10:100, the CO<sub>2</sub> pressure from 2 to 4 atm, and

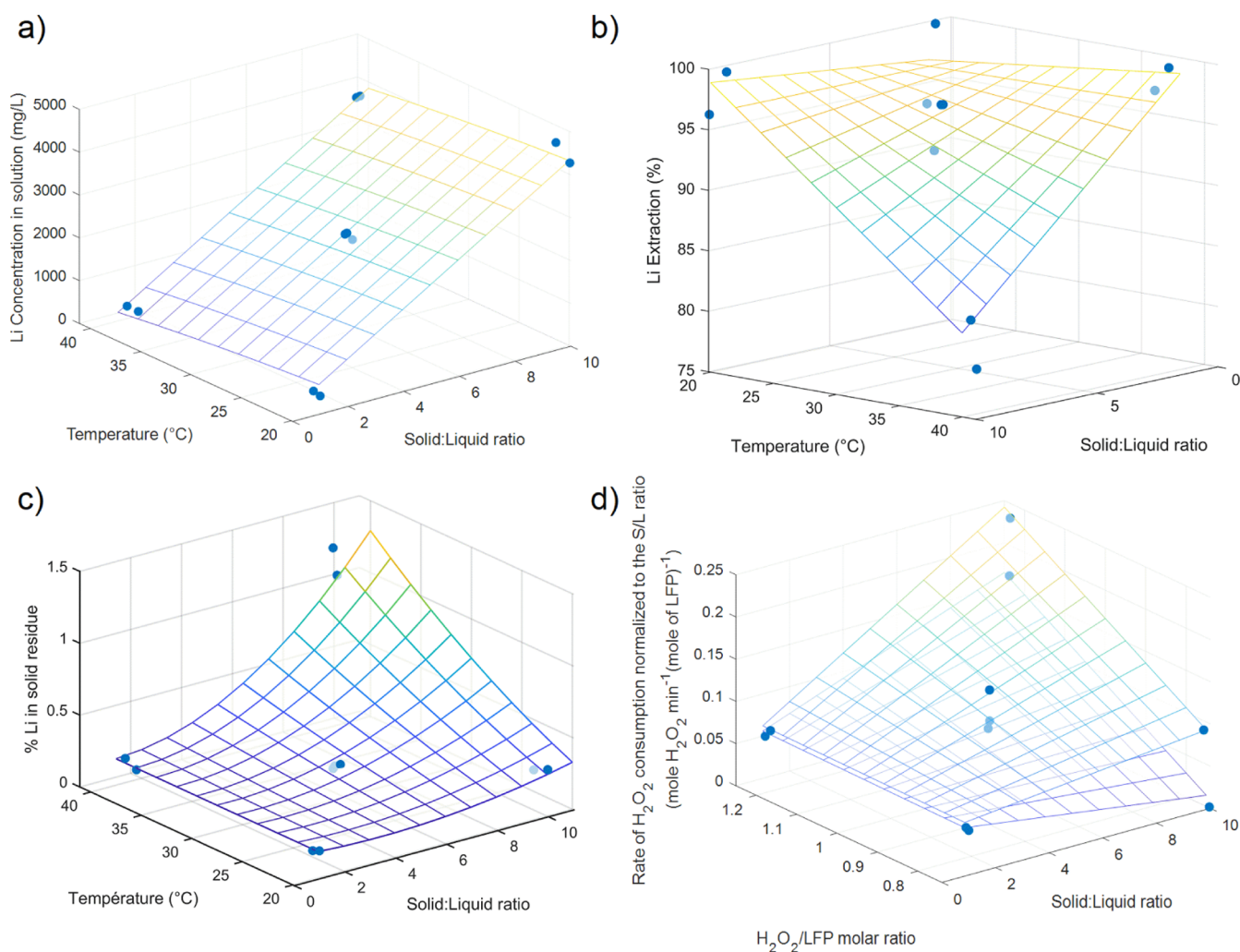


**Figure 2.** (a) Influence of S/L ratio and temperature on concentration of Li in solution; (b) influence of S/L ratio and temperature on Li percent extraction; (c) influence of S/L ratio and temperature on remaining Li concentration in FP product; influence of S/L ratio, H<sub>2</sub>O<sub>2</sub> to LFP molar ratio, and temperature (lower mesh corresponds to 20 °C; upper mesh corresponds to 40 °C) on the rate of H<sub>2</sub>O<sub>2</sub> consumption.

the molar ratio of H<sub>2</sub>O<sub>2</sub>/LFP from 0.75 to 1.25. Table 1 provides experimental results from the orthogonal experimental design including the variable conditions. A summary of main effects and interactions is shown in Table 2. The parameter values for each equation are listed in Tables S6–S9 in the Supporting Information. The XRD spectra of the final product for each test are presented in Figure S1 in the Supporting Information. They reveal a high-purity FePO<sub>4</sub> product for most tests in agreement with the Li extraction data. A comparison of the results from the three replicates, shown in Figure S2 in the Supporting Information, demonstrates a good reproducibility of the delithiation tests. The chemical assays of the filtrates are shown in Table S5 in the Supporting Information.

The main factors that affect the concentration of lithium in solution (Figure 2a) are the S/L ratio and the temperature. While the former variable has a very strong linear influence, the temperature shows an inversely proportional effect. This agrees with the inverse relationship of solubility of lithium carbonate<sup>22</sup> and CO<sub>2</sub> in water<sup>23</sup> with temperature. Hence, an increase in process temperature will reduce both the solubility of Li and the concentration of bicarbonate ion available for lithium complexation.<sup>17</sup> In the range tested, an increase in CO<sub>2</sub> pressure as well as an increase in the H<sub>2</sub>O<sub>2</sub>/LFP molar ratio

did not have a significant effect on final Li concentration in solution.

Extraction of Li is also influenced by the S/L ratio and the primary interaction between S/L ratio and temperature. Figure 2b shows the response surface of the model. To obtain a more realistic model, the experimental lithium extraction values were capped to 100%. The Li extraction shows a steep inflection point upon an increase of slurry density and temperature, reaching the lowest point at 40 °C and 10:100 S/L ratio. Above the inflection, the percent Li recovery reaches a plateau ranging from 97 to 99%. Although the model fitting is relatively low for this response ( $R^2 = 88.3\%$ ), we believe that the proposed model gives the best fit that can be obtained from the data before overfitting the model. In that sense, additional experimentations would be required to determine the interaction of less significant parameters like the initial peroxide to LFP ratio and CO<sub>2</sub> pressure on the main parameters.

The remaining concentration of Li in the FP product is an indication of delithiation reaction extent and the presence of Li bearing contaminants. The residual Li content was determined by chemical assays as described in the experimental section. The model obtained from linear regression, shown in Figure 2c, indicates that the weight fraction of Li in FP is a function of

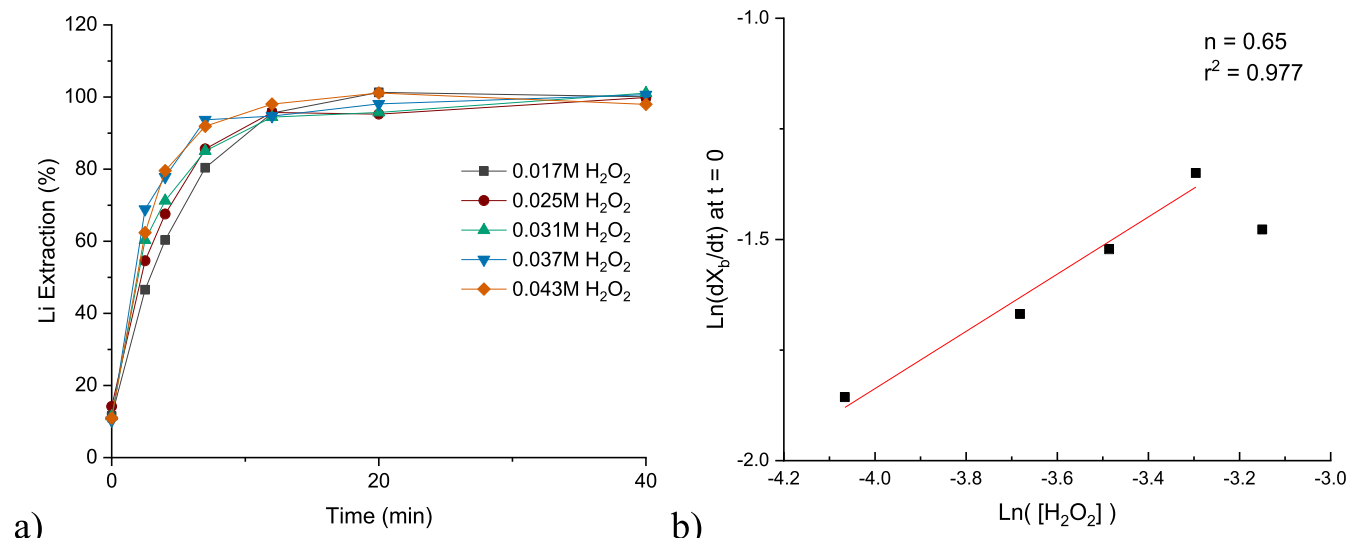


**Figure 3.** (a) Influence of H<sub>2</sub>O<sub>2</sub> concentration on reaction rate; (b) order of LFP delithiation reaction with respect to H<sub>2</sub>O<sub>2</sub> concentration. The tests were done at 25 °C, 2 atm partial pressure of CO<sub>2</sub>, a constant agitation of 1200 rpm, and an S/L ratio of 0.5:100.

S/L ratio and the quadratic interaction between both S/L ratio and temperature. This is most probably explained by the enhanced destruction of peroxide with temperature and H<sub>2</sub>O<sub>2</sub> concentration. Hence, a faster peroxide destruction leads to a lower LFP oxidation yield.

In this context, the consumption rate of H<sub>2</sub>O<sub>2</sub> (in mol L<sup>-1</sup> min<sup>-1</sup>) was also examined in relation to the four parameters studied. To alleviate the influence of the S/L ratio, the consumption rate was divided by the initial molar concentration of LFP, resulting in a rate normalized to the S/L ratio [expressed in mol H<sub>2</sub>O<sub>2</sub> min<sup>-1</sup> (mol LFP)<sup>-1</sup>]. The main factors influencing the consumption rate of H<sub>2</sub>O<sub>2</sub> are the S/L ratio, the H<sub>2</sub>O<sub>2</sub> to LFP molar ratio, and the temperature. It was found that these last two parameters are both interacting with the S/L ratio. Hence, at a low S/L ratio, both the temperature and the initial molar ratio of H<sub>2</sub>O<sub>2</sub> to LFP have little influence on the rate of H<sub>2</sub>O<sub>2</sub> destruction, while at an increased slurry density, the rate increases with temperature and peroxide to LFP ratio. These findings are in agreement with the literature in which the H<sub>2</sub>O<sub>2</sub> destruction is accelerated by its concentration, the temperature, and the solids loading of the suspension.<sup>24,25</sup> Figure 2d illustrates these relations. Note that CO<sub>2</sub> pressure was not a significant parameter in the range studied.

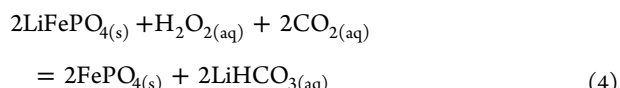
**3.2.1. Optimal Conditions.** In the range of conditions studied, the S/L ratio is clearly the most influential parameter. From an industrial perspective, this factor must be maximized in order to reduce the reactor volume and the concentration of Li in solution. The operating temperature plays a secondary role by reducing the solubility of Li and increasing the destruction of H<sub>2</sub>O<sub>2</sub>. The initial H<sub>2</sub>O<sub>2</sub> to LFP molar ratio is related to an increase of the consumption rate of peroxide, in conjunction with the S/L ratio and the temperature. The CO<sub>2</sub> pressure has not been identified as a significant parameter within the range of conditions studied. This can be explained by the fact that bicarbonate ions have always been in large excess in these experimental conditions, leaving enough room for all the lithium to be extracted from the LFP before reaching the Li solubility limits. As a matter of fact, the maximum lithium concentration in solution attained during the DOE is 4625 mg L<sup>-1</sup> of Li, which corresponds to close to 50% of the

solubility limit obtained at 2 atm CO<sub>2</sub> with pure Li<sub>2</sub>CO<sub>3</sub> (9500 mg L<sup>-1</sup>), as shown in a previous paper.<sup>17</sup>

In comparison to the previous study, the DOE allowed to increase the lithium extraction at a high S/L ratio (10:100) from 85% to close to 100%. This has been done by maintaining the reactor temperature at 20 °C, the CO<sub>2</sub> partial pressure at 2 atm, and a H<sub>2</sub>O<sub>2</sub> to LFP molar ratio of 1.25. We believe our process to be greener than others as it uses a significantly lower amount of H<sub>2</sub>O<sub>2</sub> (a green oxidant) than previous works, it employs low-pressure CO<sub>2</sub> (an inert gas highly available) that does not generate waste, and it yields FePO<sub>4</sub> amenable to direct recycling. Moreover, the process described in this work is characterized by high extraction yield, fast kinetics, and advantageous scalable process parameters (a moderately high S/L ratio and near ambient temperature).

### 3.3. Selective Leaching Kinetics and Mechanisms.

The selective delithiation of LFP with CO<sub>2</sub> and H<sub>2</sub>O<sub>2</sub> is supposed to follow this reaction



For such a heterogeneous reaction, the rate for the element Li extraction is defined as

$$\mathfrak{R}_{\text{Li}} = \frac{1}{S} \frac{dN_{\text{Li}}}{dt} \quad (5)$$

where S denotes the surface area of LFP and N<sub>Li</sub> denotes the number of Li moles at time t. The rate can also be expressed in terms of Li concentration (denoted r in the following sections) by multiplying both sides of the equation by the surface area of the solid reactant per unit of volume of liquid ( $a_s \text{ m}^2 \text{ m}^{-3}$ ).

The global rate of reaction  $r_0$  is limited by the slowest rate of the delithiation process steps. In a well-agitated reactor, four reaction steps are expected to occur: the mass transfer of species at the gas–liquid interface ( $r_{g/l}$ ), the mass transfer at the liquid–solid interface ( $r_{l/s}$ ), the mass transfer within the porous product (solid diffusion) ( $r_D$ ), and finally the chemical reaction itself ( $r_S$ ). Rates for the individual reaction steps [mol (L·s)<sup>-1</sup>] can be found in the Supporting Information.

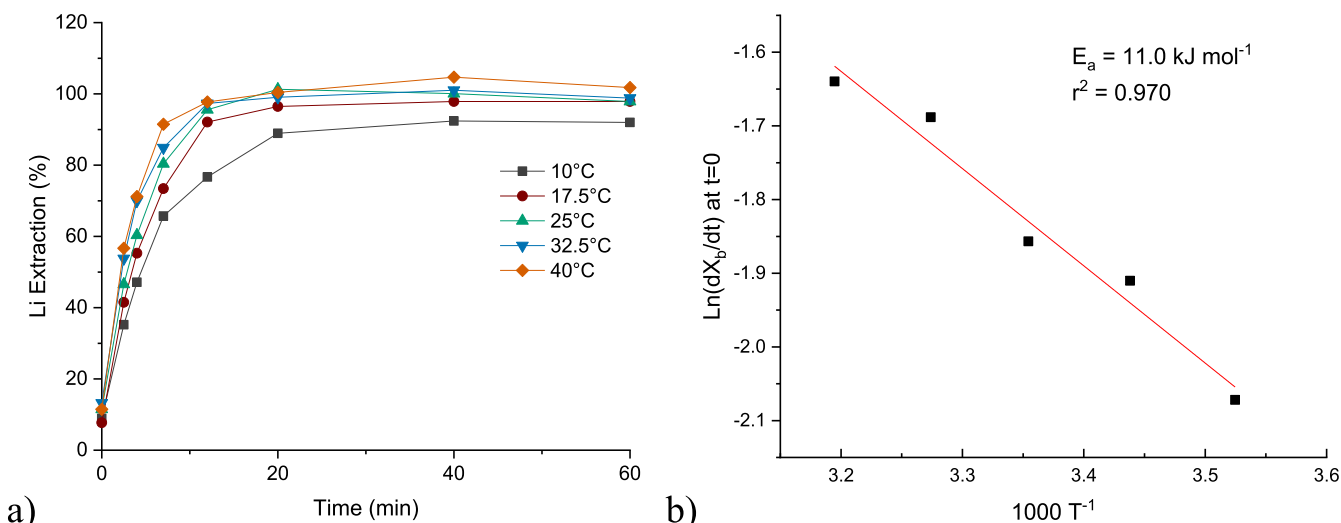


**Figure 4.** (a) Lithium extraction percentage (%) from  $\text{LiFePO}_4$  at various temperatures; (b) Arrhenius plot from the logarithm of the reaction rate versus the reciprocal of temperature. The results were obtained at a constant  $\text{CO}_2$  partial pressure of 2 atm, an S/L ratio of 0.5:100, 1200 rpm agitation speed, and an overall  $\text{H}_2\text{O}_2/\text{LFP}$  ratio of 1.43.

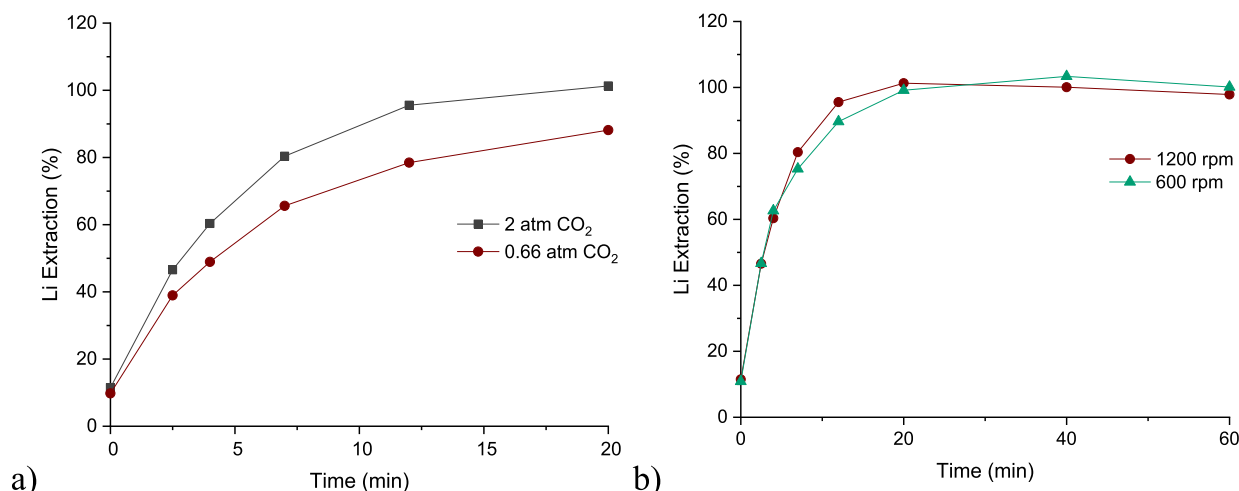


**Figure 5.** (a) Impact of decreasing the partial pressure of  $\text{CO}_2$  to 0.66 atm; the tests were done at  $25^\circ\text{C}$ , 2 or 0.66 atm partial pressure of  $\text{CO}_2$ , a constant agitation of 1200 rpm, an S/L ratio of 0.5:100, and a ratio of  $\text{H}_2\text{O}_2/\text{LFP}$  of 0.56; the influence of agitation speed on Li extraction at 2 atm partial pressure of  $\text{CO}_2$ .

At steady state, the individual rates are equal. Hence

$$r_{g/1} = r_{l/s} = r_D = r_S \quad (6)$$

Hence, the global rate is linked to the concentration of species through the global rate constant  $k_0$

$$r_0 = k_0 a_s C_{\text{bulk}} \quad (7)$$

where  $k_0$  ( $\text{m s}^{-1}$ ) is the global rate constant,  $a_s$  ( $\text{m}^2 \text{ m}^{-3}$ ) is the surface area of the solid reactant per unit of volume of liquid, and  $C_{\text{bulk}}$  is the bulk concentration of species of interest in the solution ( $\text{mol L}^{-1}$ ).

Considering that the reaction is dependent on two aqueous reactants, namely,  $\text{H}_2\text{O}_2$  and  $\text{CO}_2$ , the rate equation can be expressed as a function of their respective concentration

$$r_{\text{Li}} = a_s k_0 [\text{H}_2\text{O}_2]^n [P_{\text{CO}_2}]^p \quad (8)$$

where  $n$  and  $p$  are the reaction orders with respect to  $\text{H}_2\text{O}_2$  and to  $\text{CO}_2$ , respectively. From this expression, it is possible to

derive the rate of conversion as follows, with  $\sigma_{\text{LFP}}$  being the specific surface of LFP ( $\text{m}^2 \text{ mol}^{-1}$ )

$$\frac{dX_b}{dt} = \frac{\sigma_{\text{LFP}} k}{1000} [\text{H}_2\text{O}_2]^n [P_{\text{CO}_2}]^p \quad (9)$$

The specific area has been measured as  $2335 \text{ m}^2 \text{ mol}^{-1}$  with BET.<sup>17</sup> This value stays relatively constant throughout the reaction, ending at  $2681 \text{ m}^2 \text{ mol}^{-1}$  for the delithiated FP product.

**3.3.1. Initial Slope Analysis.** The intrinsic rate constant ( $k$ ) can be estimated from the slope of the fractional conversion at  $t = 0$ . Assuming that the mechanism is the same at various reactant concentrations, a plot of  $\ln(dX_b/dt)$  versus the logarithm of the concentration of each reactant will result in a straight line with a slope of the exponent ( $n$  or  $p$ ). For constant values of  $\text{CO}_2$  pressure, the value of  $n$  exponent has been determined from five different concentrations of  $\text{H}_2\text{O}_2$ , as shown in Figure 3a,b. Interestingly, the plot diverges from linearity at the highest concentration of peroxide, which reveals

a change in reaction mechanisms. This is expected since a high concentration of  $\text{H}_2\text{O}_2$  will promote its destruction reaction.<sup>24,25</sup> Therefore, excluding the highest concentration of peroxide, a slope of 0.65 is obtained, which is close to half-order with respect to  $\text{H}_2\text{O}_2$ .

The global rate constant  $k_0$ , which corresponds to the experimental observations, can be related to the temperature through the Arrhenius equation

$$k_0 = A'e^{-E_A/RT} \quad (10)$$

where  $A'$  is the pre-exponential factor and  $E_A$  is the activation energy. By plotting the logarithm of kinetic constant versus  $1/T$ , the dominant reaction mechanism can be determined. As a matter of fact, the slope of this plot corresponds to the activation energy of the reaction. A variation of the slope with the temperature indicates a change in the dominant mechanism. Indeed, when the activation is higher than  $40 \text{ kJ mol}^{-1}$ , the process is controlled by surface reaction. Inversely, an activation energy lower than  $15 \text{ kJ mol}^{-1}$  is diffusion-controlled, while activation energies between these values reveal a mixed controlled mechanism. Figure 4a shows the variation of Li extraction (%) with time at five different temperatures ( $10, 17.5, 25, 32.5$ , and  $40^\circ\text{C}$ ). The initial extraction of about 10.5% Li is mostly associated with the dissolution of  $\text{Li}_3\text{PO}_4$  phase present in the sample by carbonic acid, as described in the previous paper.<sup>17</sup> Final Li extractions range between 96 and 100% after 60 min.

The activation energy determined from initial slope analysis obtained at a constant concentration of  $\text{H}_2\text{O}_2$  and a constant pressure of  $\text{CO}_2$  is  $11.0 \text{ kJ mol}^{-1}$  (Figure 4b). When the partial pressure of  $\text{CO}_2$  is decreased from 2 to  $0.66 \text{ atm}$ , the reaction slows down as can be seen in Figure 5a. From the reaction order with respect to  $\text{H}_2\text{O}_2$ , the specific area, and the  $E_a$ , it is possible to derive the pre-exponent factor ( $A'$ ) and the reaction order with respect to  $\text{CO}_2$  pressure by fitting these values with a minimized sum of square error between the measured rate and predicted rate (as shown in Figure S3 in the Supporting Information). Hence, a pre-exponent factor of  $72 (\text{mol L}^{1-n} \text{ atm}^{1/p} \text{ m min}^{-1})$  and a reaction order of 0.06 with respect to  $\text{CO}_2$  were found. Therefore, the conversion rate equation can be expressed as follows

$$\frac{dX_b}{dt} = 72 \cdot \frac{2335}{1000} \cdot \exp\left(\frac{-11.0 \text{ kJ mol}^{-1}}{RT}\right) [\text{H}_2\text{O}_2]^{0.65} [\text{CO}_2]^{0.06} \quad (11)$$

Figure 5b demonstrates that agitation speed has an insignificant effect on delithiation kinetics; therefore, the diffusion of reactants through the liquid-phase boundary layer is not a limiting mechanism.

**3.3.2. Shrinking-Core Model.** Frequently in hydrochemical processes, the leaching reaction creates a solid porous product layer on the reacting particles permeable to the aqueous ions. The porous product layer thickness increases as the reaction progresses, leaving an unreacted core that shrinks until reaction completion. The overall heterogeneous process is characterized by three main reaction steps: (1) the mass transfer of reactants through the boundary layer, (2) the internal diffusion of ions through the porous layer, and (3) the chemical reaction at the interface. The simple shrinking-core model (SCM) is valid if the particles are taken to be dense, quasi-spherical, and isometric, and the reaction interface shrinks uniformly. During

experimentation, the reactant concentration shall be kept constant to minimize the influence of diffusion phenomena in the solution, and the temperature as well as agitation shall be controlled at a constant value. Thus, the S/L was kept very low (0.5:100), the partial pressure of  $\text{CO}_2$  was maintained, and  $\text{H}_2\text{O}_2$  was added in several doses to maintain approximately constant its concentration throughout the reaction. It was shown in a previous publication that the LFP does not shrink significantly during the process.<sup>17</sup> Thus, the limiting mechanism can be determined from variation of lithium extraction (change of reactant core volume) with time. The lithium extractions obtained at different temperatures were normalized ( $X_b$ ) so that the extraction yield is nil at time 0 and is 100% at maxima. In the following sections, the SCM equations relating to the chemical reaction-limited mechanism or the product layer diffusion-limited mechanism are discussed with relevant experimental data. The case of external (through the boundary layer) diffusion is discussed in the Supporting Information.

**3.3.2.1. Surface Chemical Reaction.** Application of the surface chemical reaction (SCR)-limited SCM eq 12 to the Li extraction (conversion expressed as  $X_b$ ) data shows relatively

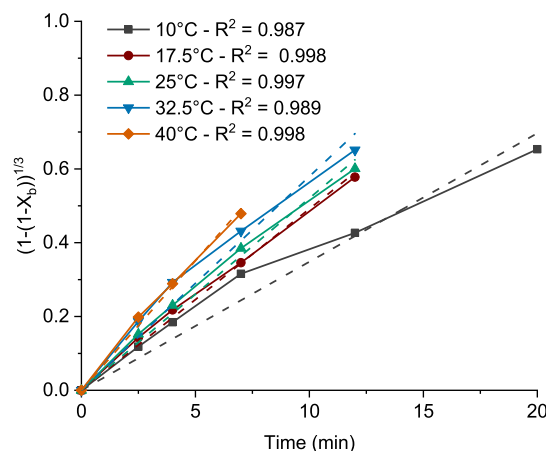


Figure 6. Plot of  $(1 - (1 - X_b)^{1/3})$  vs time at different temperatures.

good fitting ( $R^2$ ) as shown in Figure 6, although some results deviate from linearity, more specifically at  $32.5$  and  $10^\circ\text{C}$

$$1 - (1 - X_b)^{1/3} = \frac{bk_r C_{Ab}}{\rho_b r} t \quad (12)$$

where  $X_b$  is the fractional conversion (%),  $b$  is the stoichiometric coefficient for LFP,  $k_r$  is the rate constant,  $C_{Ab}$  is the bulk concentration of  $\text{H}_2\text{O}_2$  ( $\text{mol cm}^{-3}$ ),  $\rho_b$  is the molar density ( $\text{mol cm}^{-3}$ ), and  $r$  is the particle radius (cm).

**3.3.2.2. Internal Diffusion.** The internal diffusion mechanism corresponds to the diffusion of species through the product layer enveloping the reactant core. The corresponding SCM for this limiting case is given by eq 13. This internal movement is characterized by the effective diffusivity ( $D_e$ ), which is related to the true diffusivity through the porosity and tortuosity of the porous layer.<sup>26</sup> For a mono-particle system of LFP, this product layer corresponds to the delithiated FP shell with lithium vacancy acting as "porosity". The lithium-electron pair corresponds to the moving species going from the inner core toward the particle surface. In the multi-particle system, the porosity corresponds rather to the void between

the agglomerated LFP particles. The  $D_e$  is therefore more complex, also including a component related to the diffusion of the reactant or the product throughout the interstices of each LFP particle

$$1 - 3(1 - X_b)^{2/3} + 2(1 - X_b) = \frac{6bD_e C_{Ab}}{\rho_b r^2} t \quad (13)$$

Based on the determined correlation coefficient values, the model shows relatively good fit for all temperatures as shown in Figure 7 except for 17.5 and 40 °C, where deviation from linearity is more obvious.

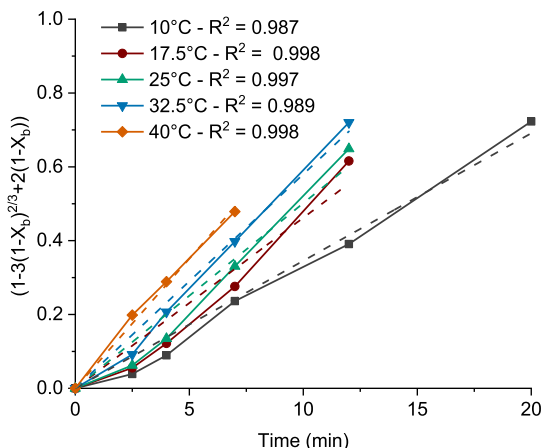


Figure 7. Plot of  $(1 - 3(1 - X_b)^{2/3} + 2(1 - X_b))$  vs time at different temperatures.

A comparison of the  $R^2$  values of the two SCM mechanisms (summarized in Table 3) indicates practically similarly good fitting with both models. Considering this ambiguity of the SCM, we may conclude that a rather mixed diffusion- and reaction-controlled mechanism applies or an altogether different mechanism that led us to the modified Avrami model Johnson–Mehl–Avrami–Kolmogorov (JMAK).

**3.3.3. Johnson–Mehl–Avrami–Kolmogorov Model.** The experimental data were also fitted to the nucleation-growth JMAK model which takes the following form

$$X_b = 1 - \exp(-K_a t)^n \quad (14)$$

where  $K_a$  is the apparent rate constant and  $n$  is a factor dependent on the geometry of the transformation for which its significance can be found in the literature.<sup>27–31</sup> The interpretation of the exponent follows this equation<sup>27,29</sup>

$$n = a + bc \quad (15)$$

where  $a$  is related to the characteristics of the nucleation steps ( $0 =$  no nucleation;  $1 =$  constant nucleation;  $>1$  increasing nucleation;  $<1$  decreasing nucleation),  $b$  is the dimension of the new phase growth, and  $c$  is the growth index which is an indication on the phase growth rate-limiting step ( $c = 1$  phase-boundary limited growth;  $c = 0.5$  diffusion-limited growth). Experimental data from delithiation in carbonic acid fit to a JMAK  $n$  factor of 1, as shown in Table 3, where the rate constant from JMAK model is compared to those of the SCM model. Accordingly, this leads to only three possibilities for the mechanisms governing the reaction.

I. Decreasing nucleation rate ( $a = 0.5$ ) with a one-dimensional (1D) phase growth ( $b = 1$ ) and a parabolic phase boundary, that is, diffusion-limited growth ( $c = 0.5$ ).

II. No nucleation ( $a = 0$ ) with a 1D phase growth ( $b = 1$ ) and a linear phase boundary, that is, phase-boundary limited growth ( $c = 1$ ).

III. No nucleation ( $a = 0$ ) with a 2D phase growth ( $b = 2$ ) and parabolic phase boundary, that is, diffusion-limited growth ( $c = 0.5$ ).

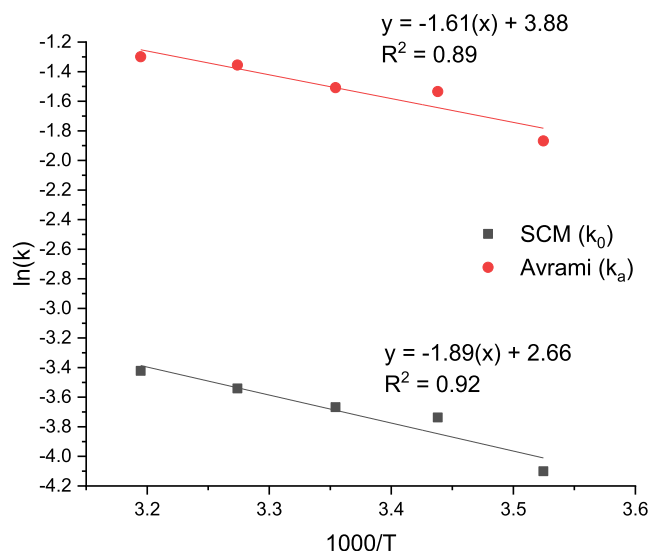
In this respect, it is impossible to distinguish one dominant mechanism based only on JMAK model. From a similar interpretation, Oyama et al. recalled the “widely accepted notion” of 1D phase-boundary motion (aligned with [100] axis) in association with channel Li diffusion in [010] axis as an argument for acceptance of the 1D phase growth controlling mechanism.<sup>27</sup> In comparison, Gupta and Koenig determined a nucleation factor  $<0$  considering a 1D phase growth ( $b = 1$ ) and diffusion-limited growth ( $c = 0.5$ ).<sup>32</sup> Inversely, Allen et al. derived a nucleation rate of 0 with a 2D phase growth ( $b = 2$ ) limited by diffusion ( $c = 0.5$ ).<sup>28</sup>

**3.3.4. Activation Energy.** Figure 8 shows the plot of Arrhenius equation based on  $K_0$  determined from SCM and on  $K_a$  from JMAK model. The activation energy determined from the global rate constant obtained from the SCM is 15.7 kJ mol<sup>-1</sup>. The activation energy calculated from rate constant obtained with the JMAK model gives 13.9 kJ mol<sup>-1</sup>, again in the same range as the SCM model. In comparison, the  $E_A$  found with the initial slope analysis is 11.0 kJ mol<sup>-1</sup>.

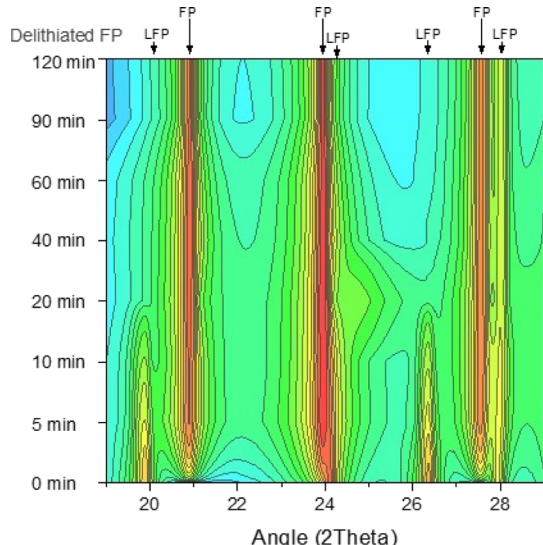
**3.3.5. Characterization.** To evaluate the evolution of phase transformation with time, samples taken during the test S-5 (refer to Table 1) were subjected to XRD analysis after rinsing with water and drying at 105 °C overnight. The results presented in Figure 9 show the evolution of the mineralogical composition versus time, starting from the pristine LFP sample to the final FP. First, the peaks related to  $\text{Li}_3\text{PO}_4$  contamination ( $2\theta = 26.0$  and 27.0° ID Card #00-015-0760)

Table 3. Rate Constants Calculated for Various Kinetic Models and Corresponding Correlation Coefficients

1000/T (1000 K <sup>-1</sup> ) [°C]	shrinking-core model						JMAK (Avrami) model		
	chemical reaction		internal diffusion		global rate constant	JMAK (Avrami) model			
	apparent rate constant ( $K_s = \frac{bk_r C_{Ab}}{\rho_b r}$ )	$R^2$	apparent rate constant ( $K_d = \frac{6bD_e C_{Ab}}{\rho_b r^2}$ )	$R^2$		apparent rate constant ( $K_a$ )	factor $n$	$R^2$	
3.52 [10]	0.0348	0.981	0.0316	0.992	0.0168	0.154	1	0.997	
3.44 [17.5]	0.0492	0.997	0.0462	0.969	0.0240	0.216	1	0.994	
3.35 [25]	0.0521	0.995	0.0502	0.979	0.0260	0.221	1	0.997	
3.27 [32.5]	0.0580	0.982	0.0580	0.993	0.0295	0.258	1	0.999	
3.19 [40]	0.0702	0.996	0.0610	0.961	0.0330	0.273	1	0.999	



**Figure 8.** Arrhenius plot of apparent kinetic constant ( $K_a$ ) determined from JMAK (red dot) and  $K_{\text{observed}}$  from SCM (gray square) vs thousand over temperature.



**Figure 9.** Contour plot of ex situ XRD spectra (Co-K $\alpha$ ) of samples taken through the delithiation of LFP [refer to test S-05 as a function of time (y-axis)].

in the LFP disappear after water immersion and pH adjustment, suggesting a complete dissolution of this compound. Considering that  $\text{Li}_3\text{PO}_4$  represents about 1.4% by weight of the sample, its solubilization would correspond to about 6% of Li extraction. In comparison, the initial Li extraction prior to reagent addition is about 11 to 12% (Figure 4a). Therefore,  $\text{Li}_3\text{PO}_4$  represents about half of the pre-leaching extraction, with the remaining 5–6% being associated with natural delithiation of the LFP upon immersion in water, as suggested by Zaghib et al.,<sup>21</sup> or the hydrolysis of an amorphous FP as suggested by Martin et al.<sup>33</sup>

After 5 min of reaction, the LFP peaks are significantly weakened and FP spectrum is already strong, revealing coexistence of both phases for a short period of time. After 20 min, the peaks associated with LFP are not visible anymore and the solid is mainly composed of FP. The contour plot shows the evolution of some characteristic peaks at  $2\theta$  angles

between 19 and 29°. While the height of the LFP peaks gradually decreases, the FP peaks increase rapidly at the beginning of the delithiation without any peak shifting related to intermediate phases, as observed by Zhang et al.<sup>34</sup>

To evaluate the degree of lithiation of individual particles, a sample considered at about 50% delithiation was subjected to STEM–electron energy loss spectroscopy (STEM-EELS) analysis. The sample was taken after 5 min of reaction from test S-06. The characterization method is described in the methodology section. Figure 10a shows the image in dark-field

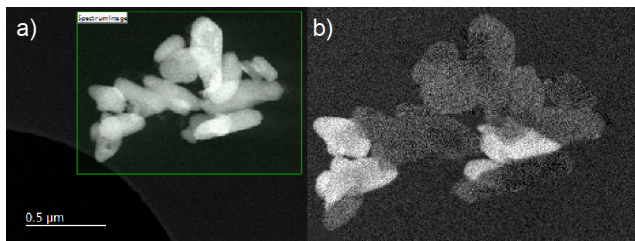


**Figure 10.** (a) Particles observed with annular dark-field detector STEM; (b) mapping of energy shift of the Fe-L3 edge of the EELS spectrum.

transmission of the particle agglomerate, and Figure 10b shows the lithiation intensity mapping where the bright zones correspond to the lithium-rich domains and the dark zones correspond to lithium-poor domains. We can see that most particles are either fully lithiated or fully delithiated, with only few particles showing both phases. This observation reveals that the delithiation is mostly controlled by nucleation of the lithium-poor phase (FP) and that this phase grows fast. This has also been observed by Chueh et al., who determined the fraction of lithium-poor, lithium-rich, and mixed particles in a 50% delithiated sample to be about 61, 36, and 3%, respectively.<sup>35</sup> Moreover, Chueh found that the degree of lithiation of a particle was not a function of the particle size, as can be observed in our sample.

#### 4. GLOBAL DISCUSSION

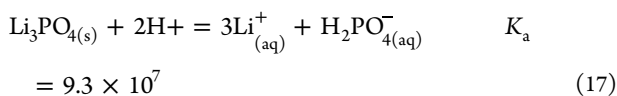
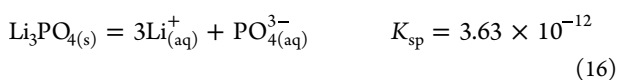
The activation energy values determined from the two modeling methods converge to similar results ranging from 13.9 to 15.7 kJ mol $^{-1}$ , which reveals, respectively, a diffusion or a mixed controlled mechanism. The initial slope analysis unveiled a slightly lower  $E_a$  at 11.0 kJ mol $^{-1}$ , which is usually more associated to diffusion-limited reaction. The activation energies found are slightly lower than the one determined by Lepage et al., who found 18.4 kJ mol $^{-1}$  after delithiation of LFP in acetic acid with H $_2$ O $_2$ .<sup>36</sup> In comparison, the activation energy found by Yang et al.<sup>11</sup> for the selective lithium extraction from spent LFP in a similar reagent scheme is 19.4 kJ mol $^{-1}$ . The values obtained by Gupta and Koenig in an unstirred chemical oxidation and electrochemical oxidation system were 125 and 21 kJ mol $^{-1}$ , respectively.<sup>32</sup> From electrochemical lithiation of FP, Allen et al. found an activation energy of 13 kJ mol $^{-1}$ .<sup>28</sup> On the other hand, Oyama et al. obtained an activation energy of 42 kJ mol $^{-1}$  after an electrochemical oxidation of LFP cathode.<sup>27</sup>

The model fittings are very good for both the JMAK and the SCM. The high linearity of the three models explored indicates a complex mechanism that involves a close correlation between chemical reactions and species diffusion. This makes difficult the selection of one specific model to represent the reaction

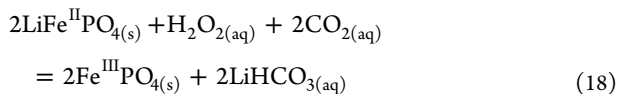
mechanism. However, by considering a nucleation-controlled mechanism as demonstrated by the image taken under STEM, the most relevant model for our process is clearly the JMAK. In this respect, the only option left for the interpretation of the JMAK exponent factor that considers the nucleation and respects the value of “*n*” found experimentally is the following: a decreasing nucleation rate (*a* = 0.5) with a 1D phase growth (*b* = 1) and a diffusion-limited growth (*c* = 0.5). This agrees with the interpretation of Gupta and Koenig.<sup>32</sup> Accordingly, a hybrid mechanism is expected to start under the nucleation-limited regime then shifting to the diffusion-limited regime, as postulated by Zhou's group and Gupta.<sup>5,32</sup> This allows to reconcile the operation of a mixed-controlled mechanism with the activation energy analysis.

Taking into consideration all the kinetics observations, the characterization, and chemical assays of the solution (Table S15 in the Supporting Information), the comprehensive reaction picture is derived to be as follows:

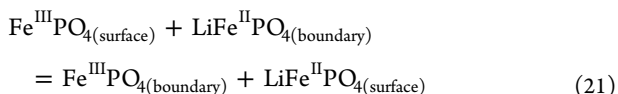
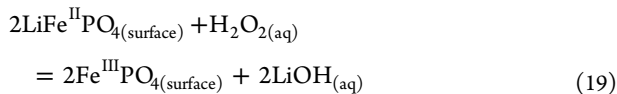
- Upon immersion in water,  $\text{Li}_3\text{PO}_4$  dissolves (reactions 16 and 17) and pH increases to around 10, within the instability region of LFP (refer to Pourbaix diagram, Figure 1). Acidification to pH 6 accelerates the dissolution of  $\text{Li}_3\text{PO}_4$ , as per reaction 17



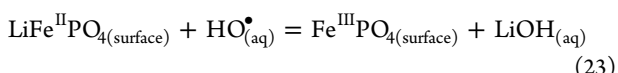
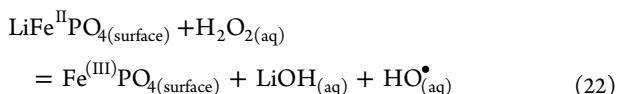
- Under pressure of  $\text{CO}_2$  and in the presence of  $\text{H}_2\text{O}_2$ , the solution reaches a strong oxidizing power exceeding the oxidation potential of the LFP ( $\text{LiFe}^{\text{II}}\text{PO}_4$ ), which as a result quickly oxidizes to FP ( $\text{Fe}^{\text{III}}\text{PO}_4$ ). The overall reaction can be summarized as per reaction 18



More specifically, we postulate the reaction to follow a three-step mechanism starting with the reduction of  $\text{H}_2\text{O}_2$  by ferrous on LFP particle surface as per reaction 19, resulting in the formation of delithiated phase nuclei and  $\text{LiOH}$  in solution. Then, the  $\text{LiOH}$  is neutralized by  $\text{CO}_2$  in solution to form  $\text{LiHCO}_3$  (reaction 20). This reaction is of great importance since an accumulation of  $\text{OH}^-$  in the vicinity of the particle surface would locally increase the pH into the instability region of FP, forming ferric hydroxide and lithium orthophosphate as indicated by the Pourbaix diagram (Figure 1). In parallel to the bicarbonate reaction, the  $\text{FePO}_4$  phase grows from the initial nuclei. Hence, the lithium ions diffuse from the internal LFP/FP phase boundary toward the surface of the particle to enter another redox cycle (reaction 21). It is generally accepted in the literature that this ionic movement occurs mostly in the [010] direction (1D).<sup>29</sup> The electrons liberated from the  $\text{Fe}^{\text{II}}/\text{Fe}^{\text{III}}$  redox couple are assumed to transit in a coupled motion with Li ions.<sup>29</sup> This movement of charge involves a transition zone behaving like a solid solution<sup>4,34,37</sup>



Ferrous iron is known as a good peroxide destruction catalyst.<sup>38,39</sup> Barb et al. proposed that this reaction follows a Fenton-like mechanism involving the generation of radicals.<sup>40</sup> We can suppose such complex reactions to take place during the delithiation of LFP as per the following reactions



We believe that the mixed-controlled mechanism identified in this study reflects a complex evolution of the rate-limiting regime as a function of delithiation extent starting with the nucleation of lithium-poor FP phase as per reaction 19 on the surface of several particles and shifting in a second time to the intra-particle lithium diffusion regime as per reaction 21.

## 5. CONCLUSIONS

Using a factorial DOE, it was possible to increase the extraction of lithium to 100% at a solid-to-liquid ratio of 10 to 100. The results from the DOE demonstrate that both S/L ratio and temperature are the most important factors affecting the four responses observed, namely, the Li concentration in the leaching solution, the efficiency of Li's extraction, the Li assays of the product, and the consumption rate of  $\text{H}_2\text{O}_2$ . This latter response was greatly affected by the initial concentration of peroxide, especially at a high solid-to-liquid ratio.

Second, the reaction kinetics have been studied by applying three different methods, namely, the initial slope analysis, the SCM, and the Avrami/JMAK model equations. In this respect, the activation energy determined from the two kinetic models converged to similar values of 15.7 and 13.9  $\text{kJ mol}^{-1}$ , respectively. Such low activation energies were associated, respectively, to diffusion or a mixed-controlled reaction. Based on the shift of the binding energy of the  $\text{Fe}^{\text{II}}/\text{Fe}^{\text{III}}$  couple measured from EELS under TEM, images of delithiated and lithiated LFP particles help confirm the JMAK equation as the most suitable kinetic model. The dual-step mechanism proposed on the basis of the JMAK model with an exponent *n* = 1 includes an initial nucleation rate-limited regime followed with the progress of the reaction with a diffusion-limited FP phase growth regime, hence agreeing with the mixed-controlled mechanism. Finally, the new delithiation process was proposed to involve a Fenton-like redox reaction between  $\text{H}_2\text{O}_2$  and LFP that triggers the nucleation of FP phase in each active particle. Then, the lithium ions diffuse through the LFP lattice toward the surface where they combine with hydroxide ions to form  $\text{LiOH}$ . This strong base is neutralized by dissolved  $\text{CO}_2$  forming soluble lithium bicarbonate ( $\text{LiHCO}_3$ ) salt, thus enabling the effective separation and recovery of extracted Li from transformed FP.

While the kinetics study demonstrated that an increase in temperature, in concentration of  $\text{H}_2\text{O}_2$ , and of  $\text{CO}_2$  pressure improves the reaction rate, the DOE showed that these parameters have a negative effect on other process parameters

such as the Li extraction percentage and the H<sub>2</sub>O<sub>2</sub> consumption. In this context, the present study gives important guiding insight to determine in a further stage of the project the optimal balance between reaction speed, process yield, and reagent consumption through economic analysis.

## ■ ASSOCIATED CONTENT

### SI Supporting Information

The Supporting Information is available free of charge at <https://pubs.acs.org/doi/10.1021/acs.iecr.2c03552>.

Additional information on feed material composition and experimental methods, additional statistic data on DOE model's parameters, description of calculation methodology of the Pourbaix diagram, calculation details and experimental data of the kinetics determination, and sample of the MATLAB program used for the process optimization modeling ([PDF](#))

## ■ AUTHOR INFORMATION

### Corresponding Authors

François Larouche – Materials Engineering, McGill University, Montreal H3A 0C5 Quebec, Canada; Centre of Excellence in Transport Electrification and Energy Storage, Hydro-Québec, Shawinigan G9N 7NS Quebec, Canada;  
 [orcid.org/0000-0003-1638-5577](https://orcid.org/0000-0003-1638-5577); Email: [francois.larouche@mail.mcgill.ca](mailto:francois.larouche@mail.mcgill.ca), [larouche.francois@hydroquebec.com](mailto:larouche.francois@hydroquebec.com)

George P. Demopoulos – Materials Engineering, McGill University, Montreal H3A 0C5 Quebec, Canada;  
 [orcid.org/0000-0001-8112-5339](https://orcid.org/0000-0001-8112-5339); Email: [george.demopoulos@mcgill.ca](mailto:george.demopoulos@mcgill.ca)

### Authors

Frédéric Voisard – Materials Engineering, McGill University, Montreal H3A 0C5 Quebec, Canada; Centre of Excellence in Transport Electrification and Energy Storage, Hydro-Québec, Shawinigan G9N 7NS Quebec, Canada

Kamyab Amouzegar – Centre of Excellence in Transport Electrification and Energy Storage, Hydro-Québec, Shawinigan G9N 7NS Quebec, Canada

Georges Houlachi – Hydro-Québec's Research Institute, Hydro-Québec, Shawinigan G9N 7NS Quebec, Canada

Patrick Bouchard – Centre of Excellence in Transport Electrification and Energy Storage, Hydro-Québec, Shawinigan G9N 7NS Quebec, Canada

Ashok Vlijh – Centre of Excellence in Transport Electrification and Energy Storage, Hydro-Québec, Shawinigan G9N 7NS Quebec, Canada

Complete contact information is available at:

<https://pubs.acs.org/10.1021/acs.iecr.2c03552>

### Funding

This study was supported by a Hydro-Québec MITACS Accelerate Fellowship and a McGill University MEDA Fellowship.

### Notes

The authors declare no competing financial interest.

## ■ ACKNOWLEDGMENTS

The authors thank Ms. Josée Pronovost for her essential contribution to this study.

## ■ REFERENCES

- (1) Padhi, A. k.; Nanjundaswamy, K. S.; Goodenough, J. B. Phospho-Olivines as Positive-Electrode Materials for Rechargeable Lithium Batteries. *J. Electrochem. Soc.* **1997**, *144*, 1188–1194.
- (2) Laffont, L.; Delacourt, C.; Gibot, P.; Wu, M. Y.; Kooyman, P.; Masquelier, C.; Tarascon, J. M. Study of the LiFePO<sub>4</sub>/FePO<sub>4</sub> Two-Phase System by High-Resolution Electron Energy Loss Spectroscopy. *Chem. Mater.* **2006**, *18*, 5520–5529.
- (3) Srinivasan, V.; Newman, J. Discharge Model for the Lithium Iron-Phosphate Electrode. *J. Electrochem. Soc.* **2004**, *151*, A1517.
- (4) Delmas, C.; Maccario, M.; Croguennec, L.; Le Cras, F.; Weill, F. Lithium Deintercalation in LiFePO<sub>4</sub> Nanoparticles via a Domino-Cascade Model. *Nat. Mater.* **2008**, *7*, 665–671.
- (5) Li, D.; Zhang, T.; Liu, X.; He, P.; Peng, R.; Wang, M.; Han, M.; Zhou, H. A Hybrid Phase-Transition Model of Olivine LiFePO<sub>4</sub> for the Charge and Discharge Processes. *J. Power Sources* **2013**, *233*, 299–303.
- (6) Thorat, I. V.; Joshi, T.; Zaghib, K.; Harb, J. N.; Wheeler, D. R. Understanding Rate-Limiting Mechanisms in LiFePO<sub>4</sub> Cathodes for Li-Ion Batteries. *J. Electrochem. Soc.* **2011**, *158*, A1185.
- (7) Bai, P.; Tian, G. Statistical Kinetics of Phase-Transforming Nanoparticles in LiFePO<sub>4</sub> Porous Electrodes. *Electrochim. Acta* **2013**, *89*, 644–651.
- (8) Sumanov, V. D.; Tyablikov, O. A.; Morozov, A. V.; Fedotov, S. S.; Vassiliev, S. Y.; Nikitina, V. A. Phase Boundary Propagation Mode in Nano-Sized Electrode Materials Evidenced by Potentiostatic Current Transients Analysis: Li-Rich LiFePO<sub>4</sub> Case Study. *Electrochim. Acta* **2021**, *368*, 137627.
- (9) Kumar, J.; Neiber, R. R.; Park, J.; Ali Soomro, R.; Greene, G. W.; Ali Mazari, S.; Young Seo, H.; Hong Lee, J.; Shon, M.; Wook Chang, D.; Yong Cho, K. Recent Progress in Sustainable Recycling of LiFePO<sub>4</sub>-Type Lithium-Ion Batteries: Strategies for Highly Selective Lithium Recovery. *Chem. Eng. J.* **2022**, *431*, 133993.
- (10) Li, L.; Bian, Y.; Zhang, X.; Yao, Y.; Xue, Q.; Fan, E.; Wu, F.; Chen, R. A Green and Effective Room-Temperature Recycling Process of LiFePO<sub>4</sub> Cathode Materials for Lithium-Ion Batteries. *Waste Manag.* **2019**, *85*, 437–444.
- (11) Yang, Y.; Meng, X.; Cao, H.; Lin, X.; Liu, C.; Sun, Y.; Zhang, Y.; Sun, Z. Selective Recovery of Lithium from Spent Lithium Iron Phosphate Batteries: A Sustainable Process. *Green Chem.* **2018**, *20*, 3121–3133.
- (12) Fan, E.; Li, L.; Zhang, X.; Bian, Y.; Xue, Q.; Wu, J.; Wu, F.; Chen, R. Selective Recovery of Li and Fe from Spent Lithium-Ion Batteries by an Environmentally Friendly Mechanochemical Approach. *ACS Sustain. Chem. Eng.* **2018**, *6*, 11029–11035.
- (13) Mahandra, H.; Ghahreman, A. A Sustainable Process for Selective Recovery of Lithium as Lithium Phosphate from Spent LiFePO<sub>4</sub> Batteries. *Resour. Conserv. Recycl.* **2021**, *175*, 105883.
- (14) Jiang, Y.; Chen, X.; Yan, S.; Li, S.; Zhou, T. Pursuing Green and Efficient Process towards Recycling of Different Metals from Spent Lithium-Ion Batteries through Ferro-Chemistry. *Chem. Eng. J.* **2021**, *426*, 131637.
- (15) Li, H.; Xing, S.; Liu, Y.; Li, F.; Guo, H.; Kuang, G. Recovery of Lithium, Iron, and Phosphorus from Spent LiFePO<sub>4</sub> Batteries Using Stoichiometric Sulfuric Acid Leaching System. *ACS Sustain. Chem. Eng.* **2017**, *5*, 8017–8024.
- (16) Jin, H.; Zhang, J.; Wang, D.; Jing, Q.; Chen, Y.; Wang, C. Facile and Efficient Recovery of Lithium from Spent LiFePO<sub>4</sub> Batteries via Air Oxidation–Water Leaching at Room Temperature. *Green Chem.* **2022**, *24*, 152–162.
- (17) Larouche, F.; Amouzegar, K.; Houlachi, G.; Bouchard, P.; Demopoulos, G. P. Conversion of LiFePO<sub>4</sub> to FePO<sub>4</sub> via Selective Lithium Bicarbonation: A Direct Pathway Towards Battery Recycling. *J. Electrochem. Soc.* **2022**, *169*, 073509.
- (18) Poling, B. E.; Thomson, G. H.; Friend, D. G.; Rowley, R. L.; Wilding, W. V. Physical and Chemical Data. In *Perry's Chemical Engineers' Handbook*; Perry, R. H., Green, D. W., Eds.; McGraw-Hill Professional Publishing, 2008.

- (19) Jing, Q.; Zhang, J.; Liu, Y.; Yang, C.; Ma, B.; Chen, Y.; Wang, C. E.-P. H. Diagrams for the Li-Fe-P-H<sub>2</sub>O System from 298 K to 473 K: Thermodynamic Analysis and Application to the Wet Chemical Processes of LiFePO<sub>4</sub> Cathode. *Material. J. Phys. Chem. C* **2019**, *123*, 14207–14215.
- (20) He, L.; Zhao, Z.; Liu, X.; Chen, A.; Si, X. Thermodynamics Analysis of LiFePO<sub>4</sub> Precipitation from Li–Fe(II)–P–H<sub>2</sub>O System at 298 K. *Trans. Nonferrous Met. Soc. China* **2012**, *22*, 1766–1770.
- (21) Zaghib, K.; Dontigny, M.; Charest, P.; Labrecque, J. F.; Guerfi, A.; Kopec, M.; Mauger, A.; Gendron, F.; Julien, C. M. Aging of LiFePO<sub>4</sub> upon Exposure to H<sub>2</sub>O. *J. Power Sources* **2008**, *185*, 698–710.
- (22) Yi, W. T.; Yan, C. Y.; Ma, P. H. Crystallization Kinetics of Li<sub>2</sub>CO<sub>3</sub> from LiHCO<sub>3</sub> solutions. *J. Cryst. Growth* **2010**, *312*, 2345–2350.
- (23) Dodds, W. S.; Stutzman, L. F.; Sollami, B. J. Carbon Dioxide Solubility in Water. *Ind. Eng. Chem. Eng. Data* **1956**, *1*, 92–95.
- (24) Yazici, E. Y.; Deveci, H. Factors Affecting Decomposition of Hydrogen Peroxide. In *Proceedings of the XIIth International Mineral Processing Symposium*; Gülsöy, Y., Ergün, S. L., Can, N. M., Çelik, B. I., Eds., 2010; pp 609–616.
- (25) Pędziwiatr, P.; Mikolajczyk, F.; Zawadzki, D.; Mikolajczyk, K.; Bedka, A. Decomposition of Hydrogen Peroxide - Kinetics and Review of Chosen Catalysts. *Acta Innov.* **2018**, *26*, 45–52.
- (26) Fuerstenau, M. C.; Han, K. N. *Principles of Mineral Processing*; Society for Mining, Metallurgy, and Exploration: Littleton, Colo., 2003.
- (27) Oyama, G.; Yamada, Y.; Natsui, R. I.; Nishimura, S. I.; Yamada, A. Kinetics of Nucleation and Growth in Two-Phase Electrochemical Reaction of Li<sub>x</sub>FePO<sub>4</sub>. *J. Phys. Chem. C* **2012**, *116*, 7306–7311.
- (28) Allen, J. L.; Jow, T. R.; Wolfenstine, J. Analysis of the FePO<sub>4</sub> to LiFePO<sub>4</sub> Phase Transition. *J. Solid State Electrochem.* **2008**, *12*, 1031–1033.
- (29) Malik, R.; Abdellahi, A.; Ceder, G. A Critical Review of the Li Insertion Mechanisms in LiFePO<sub>4</sub> Electrodes. *J. Electrochem. Soc.* **2013**, *160*, A3179–A3197.
- (30) Blázquez, J.; Manchón-Gordón, A.; Ipus, J.; Conde, C.; Conde, A. On the Use of JMAK Theory to Describe Mechanical Amorphization: A Comparison between Experiments, Numerical Solutions and Simulations. *Metals* **2018**, *8*, 450.
- (31) Christian, J. W. Formal Theory of Transformation Kinetics. In *The Theory of Transformations in Metals and Alloys*; Christian, J. W., Ed.; Elsevier, 2002; pp 529–552.
- (32) Gupta, D.; Koenig, G. M. Analysis of Chemical and Electrochemical Lithiation/Delithiation of a Lithium-Ion Cathode. *Material. J. Electrochem. Soc.* **2020**, *167*, 020537.
- (33) Martin, J. F.; Cuisinier, M.; Dupré, N.; Yamada, A.; Kanno, R.; Guyomard, D. More on the Reactivity of Olivine LiFePO<sub>4</sub> Nanoparticles with Atmosphere at Moderate Temperature. *J. Power Sources* **2011**, *196*, 2155–2163.
- (34) Zhang, X.; van Hulzen, M.; Singh, D. P.; Brownrigg, A.; Wright, J. P.; van Dijk, N. H.; Wagemaker, M. Rate-Induced Solubility and Suppression of the First-Order Phase Transition in Olivine LiFePO<sub>4</sub>. *Nano Lett.* **2014**, *14*, 2279–2285.
- (35) Chueh, W. C.; El Gabaly, F.; Sugar, J. D.; Bartelt, N. C.; McDaniel, A. H.; Fenton, K. R.; Zavadil, K. R.; Tyliszczak, T.; Lai, W.; McCarty, K. F. Intercalation Pathway in Many-Particle LiFePO<sub>4</sub> Electrode Revealed by Nanoscale State-of-Charge Mapping. *Nano Lett.* **2013**, *13*, 866–872.
- (36) Lepage, D.; Sobh, F.; Kuss, C.; Liang, G.; Schougaard, S. B. Delithiation Kinetics Study of Carbon Coated and Carbon Free LiFePO<sub>4</sub>. *J. Power Sources* **2014**, *256*, 61–65.
- (37) Bai, P.; Cogswell, D. A.; Bazant, M. Z. Suppression of Phase Separation in LiFePO<sub>4</sub> Nanoparticles during Battery Discharge. *Nano Lett.* **2011**, *11*, 4890–4896.
- (38) Messele, S. A.; Bengoa, C.; Stüber, F. E.; Giralt, J.; Fortuny, A.; Fabregat, A.; Font, J. Enhanced Degradation of Phenol by a Fenton-Like System (Fe/EDTA/H<sub>2</sub>O<sub>2</sub>) at Circumneutral pH. *Catalysts* **2019**, *9*, 474.
- (39) Jones, C. W.; Clark, J. H. Activation of Hydrogen Peroxide Using Inorganic and Organic Species. In *Applications of Hydrogen Peroxide and Derivatives*; Jones, C. W., Clark, J. H., Eds.; The Royal Society of Chemistry, 1999; pp 37–78.
- (40) Barb, W. G.; Baxendale, J. H.; George, P.; Hargrave, K. R. Reactions of Ferrous and Ferric Ions with Hydrogen Peroxide. *Nature* **1949**, *163*, 692–694.

**CAS BIOFINDER DISCOVERY PLATFORM™**

**ELIMINATE DATA SILOS. FIND WHAT YOU NEED, WHEN YOU NEED IT.**

A single platform for relevant, high-quality biological and toxicology research

**Streamline your R&D**

**CAS** A division of the American Chemical Society